Facile fabrication of carbon dots containing abundant h-BN/graphite heterostructures as efficient electrocatalyst for hydrogen peroxide synthesis

Qixin Yuan [a], Mengmeng Fan [a,b,*], Yuying Zhao [b], Jingjie Wu [c], Jithu Raj [c], Zeming Wang [d], Ao Wang [b], Hao Sun [b], Xiang Xu [a], Yuhan Wu [a], Kang Sun [b,**], Jianchun Jiang [b,**]

[a] *Jiangsu Co-Innovation Center of Efficient Processing and Utilization of Forest Resources, International Innovation Center for Forest Chemicals and Materials, College of Chemical Engineering, Nanjing Forestry University, Nanjing 210037, China*
[b] *Key Lab of Biomass Energy and Material, Jiangsu Province, Jiangsu Co-Innovation Center of Efficient Processing and Utilization of Forest Resources, Institute of Chemical Industry of Forest Products, Chinese Academy of Forestry, Nanjing, 210042,China*
[c] *Department of Chemical and Environmental Engineering, University of Cincinnati, Cincinnati, OH 45221, USA*
[d] *Institute of Nanochemistry and Nanobiology, School of Environmental and Chemical Engineering, Shanghai University, Shanghai 200444, China*

ABSTRACT

Carbon dots with hexagonal boron nitride/graphite (h-BN/G) heterostructure are prepared and used as an efficient electrocatalyst for hydrogen peroxide synthesis by 2 e⁻ oxygen reduction reaction (ORR). This abundant heterostructure are fabricated by sucrose-assisted h-BN exfoliating followed by graphite growing progress. The catalytic activity of the carbon dots is superior to the reported carbon-based electrocatalysts in an alkaline environment, with the achieved selectivity of 88%− 95% at 0.45–0.75 V vs. RHE, the mass activity of 960 mmol $g_{catalyst}^{-1}$ h^{-1} and over 90% Faradaic efficiency. The experimental results and density functional theory simulation demonstrate that the h-BN/G heterostructure possesses outstanding catalytic performance to 2 e⁻ ORR, and the electron-deficient B atoms at the heterostructure act as the key active sites. This research emphasizes the promise of heterostructure in highly efficient carbon-based electrocatalyst and provides a facile method for fabricating other heterostructures.

1. Introduction

Hydrogen peroxide (H_2O_2) is one of the most widely-used chemicals, especially as a green oxidant and bleaching agent for waste treatment and the paper industry [1,2]. However, the traditional "anthraquinone oxidation" method has the disadvantages of high energy consumption and organic waste generation, which contradict the energy and environment crisis[3]. Recently, more attention was focused on a green method of electrochemically synthesizing H_2O_2 by reducing O_2 (oxygen reduction reaction, ORR) in a 2 e⁻ pathway[4,5]. Currently, the key challenges are the design and synthesis of highly efficient electrocatalysts to realize the large-scale industrial application of electrochemical H_2O_2 synthesis technology [6].

Carbon-supported metal catalysts have over 90% H_2O_2 selectivity (calculated by a rotating ring-disc electrode measurement) to HO_2^-/H_2O_2 with expensive precious metals[7–10] and transition metals[11–15]

dispersed on heteroatom-doped carbon material, for example, single Mo atoms dispersed in N-doped carbon showing ∼ 95% HO_2^- selectivity in the alkaline environment [14]. Compared to the complicated modulating factors in the carbon-supported metal catalysts (e.g., metal size, metal valence, loading mass, and doped heteroatoms), metal-free carbon materials are the more promising alternatives due to their abundant reserves, and tunable and stable structures. Currently, heteroatoms doping is the most general method for modulating carbon-based electrocatalysts including N[16], B[17], and O[18]. Meanwhile, edge or defect structures also can act as the active sites[19,20]. Nevertheless, the heteroatoms- doped carbon electrocatalysts still suffer from the low catalytic activity and high overpotential toward 2 e⁻ ORR, which inspires us to explore new modulating methods.

Fabricating heterostructures is a new modulating route to create catalytic sites in carbon-based electrocatalysts, for example, in the heterostructure of boron carbon nitride nanosheets/fullerene molecules,

the interfacial electronic environment induces highly active catalytic sites in oxygen evolution reaction and ORR[21]. Similarly, hexagonal boron nitride (h-BN, called "white graphite") and graphite (G) have greatly similar atomic arrangements, but they have totally different electronic properties[22]. Theoretically, the heterostructure of h-BN/G can modulate the electronic environment of interfacial atoms' (B, N, C) electronic environment[23] by regulating h-BN domain size or h-BN/G ratio[24]. Accordingly, we can speculate that the appropriate interfacial electronic environment in h-BN/G heterostructure can induce high activity and selectivity toward 2 e⁻ ORR.

Among the various topological nanostructures in carbon nanomaterials, quantum dots or carbon dots emerge as nanometer-sized zero-dimensional substrates featured with an enriched density of edge sites [25,26]. Many heteroatoms doped graphene quantum dots have greatly enhanced catalytic performance due to the abundant edge active sites. Therefore, edge sites of these quantum/carbon dots subjected to h-BN/G heterostructure functionalization can generate HO_2^-/H_2O_2 [22].

Here, we prepared h-BN nanodots as the "seed nucleation" by a sucrose-assisted exfoliation method. Then, the grafted sucrose molecules to the edge of "seed nucleation" grew into graphite domains, then leading to the formation of h-BN/G heterostructure[27]. The catalytic performance of carbon dots with h-BN/G heterostructure (BN-C) was measured by adding a conductive substrate (reduced graphene oxide, rGO)[28]. The BN-C possesses an enriched density of heterostructure sites and exhibits over 90% selectivity toward HO_2^- in the alkaline environment and enhanced stability (95% retention after 12 h testing), superior to the reported carbon-based catalysts. Moreover, the assembled flow cell setup shows a high production rate of HO_2^- (960 $mmol\,g_{catalyst}^{-1}\,h^{-1}$) and Faradaic efficiency (over 90% at the first 4-h testing). Density functional theory (DFT) suggests the high activity primarily originates from the h-BN/G heterostructure at the edge.

2. Experimental section

2.1. Synthesis of pBN

Firstly, boric acid (0.62 g), dicyandiamide (2.7 g) was dispersed into 50 ml deionized water in a 200 ml beaker, and then the above solution was sonicated for 1 h. Secondly, the solution was fiercely stirred and heated on a hot plate until all water completely evaporated. Thirdly, the obtained solid was ground into powders in a mortar and then calcined at 800 °C for 0.5 h under NH_3 (50 sccm) in a resistance-heating horizontal furnace. After cooling to room temperature, we can get the powders of pBN.

2.2. Synthesis of BN-S dots

The pBN (0.6 g) and sucrose (3.0 g) were added into a 200 ml ball milling jar and the mixture was milled for 10 h. The mixture was dispersed into the mixing solution (volume ratio of isopropanol (IPA): H_2O= 1: 1) with a concentration of 10 mg ml⁻¹. After sonication for 5 h (200 W), the solution was centrifuged for 30 min at 3000 rpm to obtain the BN-S suspension.

2.3. Synthesis of BN-C/rGO, BN-C, rGO

GO was dispersed into a solution of IPA/H_2O= 1:1 with a concentration of 1.0 mg ml⁻¹. The BN-S suspension (6 ml) and GO solution (10 ml) were mixed by sonication for 2 h (200 W). The mixing solution was transferred into a 25 ml stainless steel autoclave and then the autoclave was heated for 24 h under 200 ℃. After cooling to room temperature, the BN-C/rGO was obtained by centrifugation at 3000 rpm for 10 min and then, the BN-C/rGO was washed three times with DI water. The BN-C/rGO was obtained by freeze-drying. The BN-C/rGO-x (x = 0.1, 0.4, 0.6, 1.0) was prepared by the same method except for adding different volume (1 ml, 4 ml, 6 ml and 10 ml) of BN-S solution to GO solution (10

ml). The BN-C and rGO were prepared by the same method but without adding GO solution and BN-S suspension, respectively.

2.4. Preparation of C/rGO, B-C/rGO, N-C/rGO, B,N-C/rGO, and pBN-C/rGO

The C/rGO was prepared by the same process as BN-C/rGO but only adding the sucrose solution into the GO solution. For preparing B-C/rGO, N-C/rGO, B,N-C/rGO, boric acid or/and dicyandiamide was firstly dissolved into sucrose solution and then the above solution 6 ml was added into 10 ml GO solution. The mixing solution was transferred into a 25 ml autoclave for hydrothermal reaction. The rest of the preparation conditions are the same as those of the BN-C/rGO.

The preparation of pBN-C/rGO was the same as the BN-C/rGO, but without the ball milling process in the preparation of BN-S solution.

2.5. Electrochemical characterization

The electrochemical tests were carried out on an electrochemical workstation (Chenhua CHI760E) by a three-electrode cell. A graphite rod and an Hg/HgO electrode were acted as the counter electrode and reference electrode, respectively. The RRDE (Pine) with a disk glassy carbon area of 0.2475 cm⁻² and a Pt ring area of 0.1866 cm⁻² was used as the working electrode. Each catalyst (2 mg) was dispersed into 1 ml solution composed of 8: 2: 1 =IPA: DI water: 5 wt% Nafion solution, and then the uniform catalyst ink was prepared by sonication (400 W, 2 h). The 10 μl ink was dropped onto the RRDE electrode and dried at room temperature. Linear sweep voltammetry (LSV) curves were conducted in O_2 saturated 0.1 M KOH solution at a scan rate of 10 mV s⁻¹ at the speed of 1600 rpm. The solution resistance (R_s) was not calibrated. The HO_2^- selectivity and electron transfer number were calculated by the following Eqs. (1–2) based on the LSV curves. A potential of 1.2 V (vs. RHE) was applied to the ring electrode.

$$HO_2^- \text{ selectivity } (\%) = 200 \times \frac{I_R/N}{I_D + I_R/N} \tag{1}$$

$$n = \frac{4|I_D|}{I_D + I_{R/N}} \tag{2}$$

Where I_R is the ring current, I_D is the disk current, and N is the collection efficiency (0.37 after calibration).

2.6. Electrochemical test in a flow cell

The test was completed using a flow cell setup in a two-compartment cell with a cation exchange membrane as the separator. The BN-C/rGO catalyst was deposited on the gas diffusion layer electrode (GDL, HESEN HCP120) (working area 1 cm²) with the loading of 1 mg cm⁻² as the cathode. The Pt film and Ag/AgCl electrode were used as the anode and reference electrodes, respectively. In two compartments, 0.1 M KOH (100 ml) was used as the electrolyte and was recycled through each respective compartment at the flow rate of 20 ml min⁻¹. The O_2 supply rate was fed at the rate of 40 ml min⁻¹ to the cathode. The electrosynthesis of HO_2^- was performed at a fixed potential of 0.2 V vs. RHE (current density of ~50 mA cm⁻²).

The Faradaic efficiency (FE%) of H_2O_2 was calculated according to the following equation:

$$FE \% = 2CVF/Q *100\% \tag{3}$$

where C represents the concentration of H_2O_2 (mol l⁻¹) in the electrolyte, V is the volume of electrolyte (l), F is the faraday constant (96485 C mol⁻¹), and Q is the total charge amount (C) passed during the reaction. The Q was determined by integral operation in the electrochemical workstation:

The H_2O_2 concentration in the electrolyte was measured by a

titration method using $Ce(SO_4)_2$. The addition of H_2O_2 leads to the conversion from yellow Ce^{4+} to colorless Ce^{3+} in the following reaction 4:

$$2Ce^{4+} + H_2O_2 = 2Ce^{3+} + 2 H^+ + O_2 \qquad (4)$$
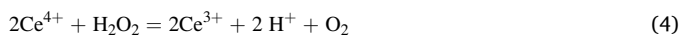
The C_{H2O2} was calculated based on Eq. 5:

$$C_{H2O2} = 1/2 \, \Delta C_{Ce4+} \qquad (5)$$

UV-Vis spectroscopy was used to make the linear calibration curve between Ce^{4+} concentration and the Ce^{4+} absorbance at 317 nm.

2.7. Characterization

The morphology was characterized by high-resolution TEM (FEI Talos F200s). Energy dispersive X-ray element mappings were performed by (FEI Super-X EDS Detector). The structure and composition were characterized by X-ray photoelectron spectra (Thermo Scientific Al K_α), X-ray diffractometer (Bruker, D8 FOCUS) equipped with a Cu K_α radiation source ($\lambda = 0.154$ nm), FT-IR (Nicolet IS10). The Raman spectra were measured by a Renishaw in Via with a 532 nm laser source.

2.8. DFT simulation

The DFT calculations were accomplished by using the Vienna Ab initio Simulation Package (VASP), carrying out the projected augmented wave (PAW) model. The exchange and correlation effect was described by the revised Perdew-Burke-Ernzerhof (RPBE) functional, within the generalized gradient approximation (GGA) approach. The cutoff energy was set to 400 eV for all the calculations. The Brillouin zone of the periodic 2D slab separated with a 15 Å vacuum space along the Z-axis was sampled with $2 \times 2 \times 1$ and $4 \times 4 \times 1$ k-points grids for geometry optimization and electronic structure calculations, respectively. The unit cell size is set at 20×20 Å to avoid interactions between the imaging cells. Fermi-smearing of $kBT = 0.1$ eV was employed to speed up the convergence.

The computational hydrogen electrode (CHE) model was used to calculate Gibbs free energy of reaction for 2 e^- ORR elementary steps, defined as $\Delta Gn (U) = \Delta Gn (U = 0)+neU$, where n is the number of e^- transferred in reaction and U is the electrode potential versus the reversible hydrogen electrode (RHE). At U= 0 V, $\Delta Gn = \Delta En - T\Delta S + \Delta ZPE$, where ΔEn is DFT-calculated reaction energy in vacuum, $T\Delta S$ is the entropy contributions to reaction at T = 298.15 K, ΔZPE is zero-point energy (ZPE) correction based on the calculated vibrational frequencies. The free energy of O_2 (g) was derived as $G_{O2(g)} = 2 G_{H2O (l)} - 2 G_{H2} - 4 \times 1.23$ eV since the high-spin ground state of an oxygen molecule is notoriously poorly described in DFT calculations.

3. Results and discussion

3.1. Morphological Characterization

We firstly prepared h-BN nanodots as "seed nucleation" through mechanochemically exfoliating porous h-BN (pBN) with a sucrose-assisted sonication process. Long-time ball milling can break pBN sheets into small sizes and, meanwhile, induce the formation of more B-C and N-C covalent bond bonding with sucrose molecules by mechanochemical reaction [29,30] as demonstrated in the Fourier Transform Infrared Spectroscopy (FT-IR) spectra (Fig. S1). After the mechanical force-induced exfoliation and centrifugation[31], the sucrose edge-grafted h-BN nanodots (BN-S dots) were separated by a centrifuge process. Then, the edge-grafted sucrose molecules act as the carbon precursor to grow into the graphite domain along the crystal structure of h-BN domain by a hydrothermal reaction (200 ℃, 24 h). As-prepared carbon dots (BN-C) contain abundant in-situ formed h-BN/G heterostructure. Meanwhile, the BN-C carbon dots were dispersed on the

conductive rGO sheets (prepared by hydrothermal reduction of GO) (Fig. 1). In the hydrothermally reducing progress, GO sheets became regionally hydrophobic due to their restored conjugated domains and diminished oxygenated functionalities[32,33]. The combination of hydrophobicity and interactions results in a 3D random stacking between flexible rGO sheets, during which the BN-C dots are dispersed and immobilized on N-rGO sheets by π-π conjugate and electrostatic interaction[34].

The pBN contains abundant pores and h-BN domains (marked with red circles) with a layer distance of 0.35 nm corresponding to the (002) plane of the h-BN domain in the High-Resolution Transmission Electron Microscopy (HR-TEM) image (Fig. 2a). In Fig. 2b, c, we can observe the even-sized BN-S nanodots with a "core-shell" structure and a narrow lateral size distribution of 5–9 nm, and the "core" and "shell" can be assigned to the h-BN domain and the grafted sucrose molecules, respectively. In the Atomic Force microscope (AFM) image, the thickness of BN-S nanodots is around 5 nm (Fig. 2d and Fig. S2). The prepared BN-C carbon dots solution shows light yellow fluorescence under 365 nm light indicating the formation of carbon dots (Fig. S3). Meanwhile, the BN-C carbon dots are effectively immobilized on rGO sheets, as demonstrated by the lighter color solution compared to the blank BN-C carbon dots without the addition of rGO (Fig. 2e). As shown in Fig. 2 f, the prepared BN-C/rGO exhibits abundant BN-C carbon dots uniformly dispersed on rGO sheet with the BN-C carbon dots having the lateral size distribution of 2–4 nm and lattice lines of ~0.22 nm corresponding to the (100) plane [26,34–36]. As shown in the High-Angle Annular Dark Field scanning transmission electron microscopy (HAADF-STEM) image and element mapping images in Fig. 2 g, the uniform B, N element distribution demonstrates the uniform distribution of BN-C carbon dots on rGO sheets. Furthermore, the abundant mesopores and open pore structure of BN-C/rGO (Fig. S4 and S5) also promote H_2O_2 formation by exposing more sites, enhancing mass transfer and shortening the resident time of HO_2^-.

Due to the structural similarity between h-BN and graphite, the crystal h-BN nanodots are beneficial to the growth of the graphite domain as demonstrated by our previous researches that the h-BN domain can epitaxially grow along the edge of graphene quantum dots to fabricate the h-BN/G heterostructure[22]. As we predicted, when no h-BN nanodots "seed nucleation" were added, there were fewer carbon dots in the solution, and the carbon dots show an amorphous structure without lattice lines (Fig. S6). We added H_3BO_3 (B precursor) and dicyandiamide (N precursor) into the sucrose/GO mixing solution to prepare B, N-C/rGO with a separated B, N dopant. Similarly, a few B, N-C carbon dots form, and the carbon dots also show an amorphous carbon structure (Fig. S7). The above morphological comparison well demonstrates the "nucleation seeds" function of h-BN nanodots on the growth of h-BN/G heterostructure[37].

3.2. Spectroscopic Characterization

In the Raman spectra (Fig. 3a), the pBN exhibits the typical peak of h-BN material at 1357 cm^{-1} indicating abundant h-BN domains[27]. The BN-C/rGO shows a slightly lower I_D/I_G ratio (the intensity ratio of D peak to G peak) than that of rGO [38] due to the doping of high crystal BN-C carbon dots with a low I_D/I_G ratio. Remarkably, compared to the D peaks of rGO and BN-C/rGO at 1336 cm^{-1}, the D peak of BN-C carbon dots is broader and red-shifted to 1362 cm^{-1}, which can be attributed to the overlap of D peak with the typical peak of pBN (at 1375 cm^{-1}). In the X-ray diffraction (XRD) patterns, the pBN has broad (002) and (100) peaks indicating the amorphous structure (namely, abundant h-BN microcrystal) as demonstrated in the HR-TEM image (Fig. 2a) [22]. The overall (002) peak of the BN-C/rGO increases to 25.8° corresponding to 0.344 nm compared to the rGO (24.6°) in Fig. 3b due to the doping of the crystal BN-C carbon dots. In the FT-IR spectra in Fig. 3c, compared to the rGO, there are obvious B-N-B and B-N peaks in the BN-C/rGO located at 790 cm^{-1} and 1350 cm^{-1}[22,31], respectively, demonstrating the
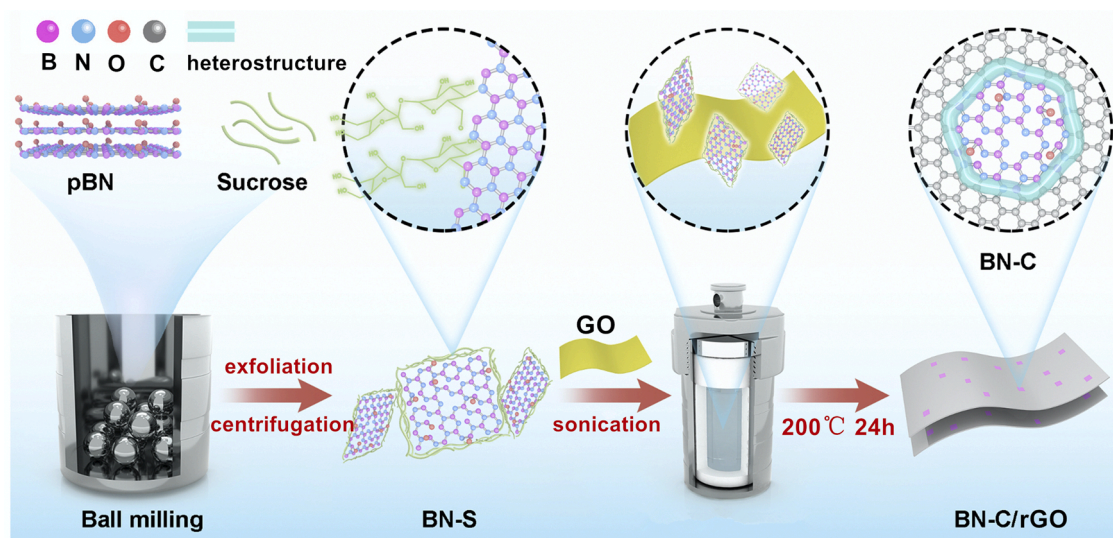
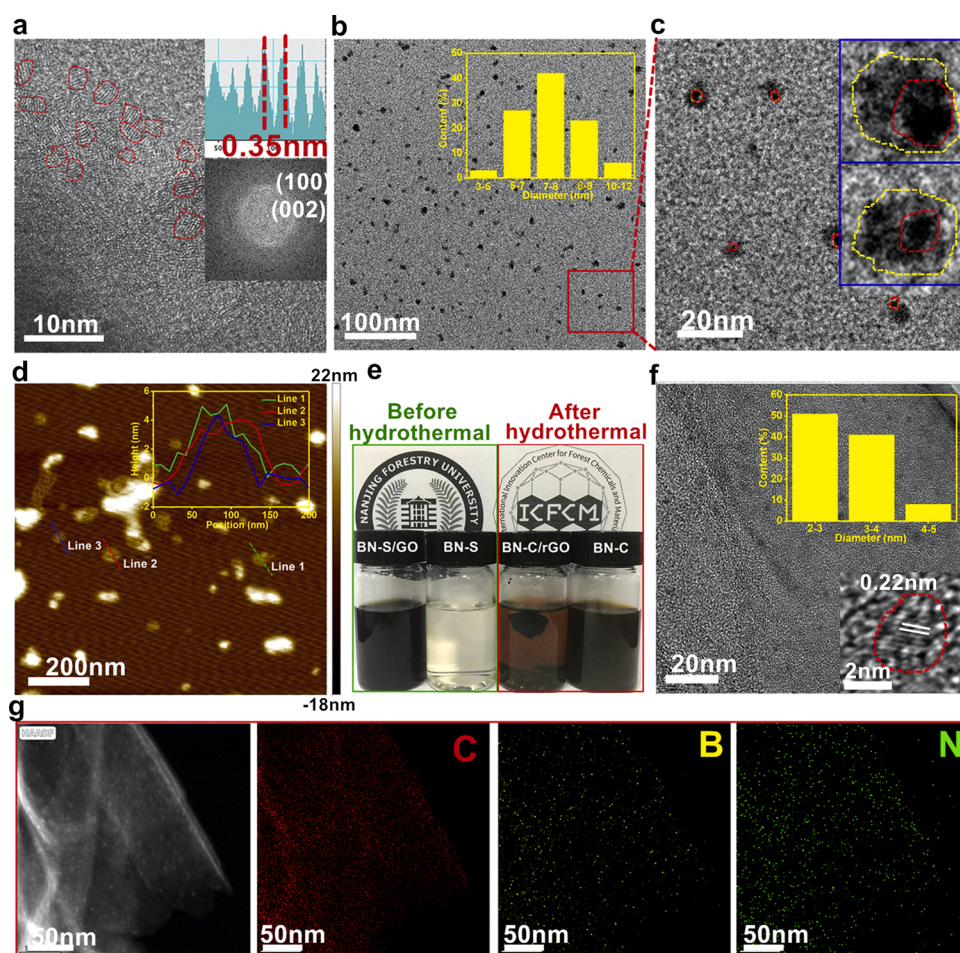**Fig. 1.** The synthetic procedure of the BN-C/rGO.

Fig. 2. (a) The HR-TEM image of pBN (inset, corresponding lattice fringes and FFT pattern), the h-BN microcrystal remarked with red circles. (b, c) The HR-TEM images of BN-S dots (inset, the size distribution, the zoom-in BN-S dots with "core (red dotted line)-shell (yellow dotted line)" structure. (d) The AFM image of BN-S dots (inset, the thickness profiles). (e) The photograph of before and after hydrothermal progress of BN-S/GO and BN-S solution. (f) The HR-TEM image of BN-C/rGO (inset, the size distribution and the HR-TEM image of BN-C carbon dots dispersed on rGO sheet). (g) The HAADF-STEM image of BN-C/rGO and the corresponding elemental mapping images of C (red), B (yellow), and N (green).

existence of h-BN domain. The enhanced B-C (at 1030 cm^{-1}) and C-N (at 1678 cm^{-1}) peak intensity[22,39] also indicate the covalent bond formation at the interface between the h-BN domain and graphite domain. The X-ray photoelectron spectroscopy (XPS) was measured to further characterize the structure and composition of the h-BN/G heterostructure. In the high-resolution C1s spectrum (Fig. 3d), compared to the

pBN (Fig. S8), the BN-C carbon dots have obviously enhanced C-B (284.0 eV) and C-N (285.3 eV) peak intensity[40] demonstrating that apart from the intrinsic C-B/C-N bonds existed in the pBN, there are many newly-formed C-B/C-N bonds in the BN-C carbon dots, which can be attributed to the formation of h-BN/G heterostructure [22,41]. In the O1s spectrum (Fig. S9, S10), the BN-C carbon dots and rGO show few
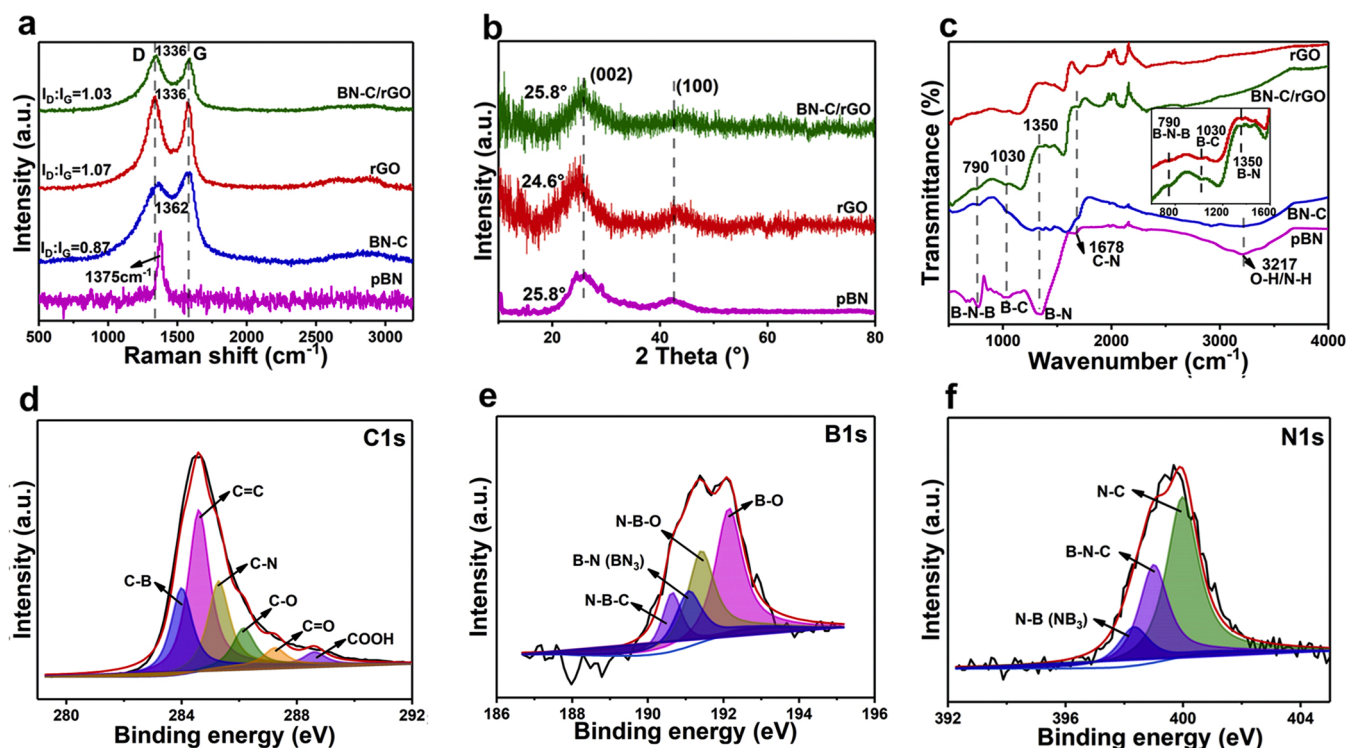
Fig. 3. (a) The Raman spectra of rGO, BN-C carbon dots, pBN and BN-C/rGO. (b) The XRD patterns of rGO, pBN and BN-C/rGO. (c) The FT-IR spectra of different samples. (d-f) The XPS high-resolution C1s, B1s and N1s spectra of BN-C carbon dots.

oxygen-containing groups (C-O at 286.1 eV, C=O at 287.2 eV, COOH at 288.6 eV). In the B1s and N1s spectra (Fig. 3e, f), the appearance of a B-N (BN_3) peak at 191.1 eV and an N-B (NB_3) peak at 398.3 eV demonstrate the existence of h-BN domains in the BN-C carbon dots[37, 42,43]. The peaks for N-B-C at 190.6 eV and B-N-C at 399.0 eV appear in B1s and N1s spectra[22], respectively, proving the presence of h-BN/G heterostructure.

3.3. Electrocatalytic performance toward HO_2^- generation

In order to compare the intrinsic 2 e⁻ activity in ORR, a standard three-electrode Rotating Ring-Disk Electrode (RRDE) was used in alkaline solution (0.1 M KOH). The electrolyte was pre-saturated with high-purity O_2, and the RRDE electrode was held at a high-speed of 1600 rpm [7,15]. The ring electrode was kept at 1.2 V vs. RHE to oxidize the produced HO_2^- (The produced H_2O_2 molecule is in the form of HO_2^- in the strongly alkaline environment) formed at the disk electrode[7]. The collection efficiency was calibrated to be 0.37 by the redox reaction of $[Fe(CN)_6]^{4-}/[Fe(CN)_6]^{3-}$ in Fig. S11 [7,44]. As shown in Fig. 4a, all catalysts show ORR polarization curves with the disk current (solid line) produced from O_2 reduction and the ring current (dashed line) from HO_2^- oxidation. The BN-C/rGO shows the highest catalytic activity with the most positive onset potential (E_{onset} determined at ring current I_R = 0.05 mA HO_2^-, corresponding to the current density J_R = 0.3 mA cm^{-2}) of 0.78 V vs. RHE, the maximal I_R up to 0.54 mA, maintaining high HO_2^- selectivity of 88%– 95% across a broad potential window of 0.45–0.75 V vs. RHE (Fig. 4a, b). Compared to the bare RRDE, the BN-C/rGO loaded on RRDE shows a much higher disk/ring current indicating the distinctly high 2 e- ORR performance (Fig. S12). The blank rGO has the catalytic activity (E_{onset}=0.75 V vs. RHE, HO_2^- selectivity=78%, I_R max=0.33 mA) due to the existence of a few oxygen species (-OH, -COOH groups) [2,18,45], The low catalytic activity of BN-C carbon dots (E_{onset}=0.60 V vs. RHE, HO_2^- selectivity ~90%, and I_R max=0.25 mA) can be attributed to the high percolation threshold value and high water-solubility during the electrochemical testing[34,46].

The electron transfer numbers of BN-C dots and BN-C/rGO are calculated to be ~2.2, close to the ideal 2.0 indicating the high HO_2^- selectivity (Fig. 4c) [14]. Compared to the BN-C (91.1 mV dec^{-1}) and the rGO (84.7 mV dec^{-1}), the BN-C/rGO has a lower Tafel slope (73.2 mV dec^{-1}) (Fig. 4d) indicating rapid ORR kinetics, which can be attributed to the synergic effect of abundant active heterostructure sites and highly conductive rGO substrate[15,20]. As shown in Fig. 4e, the BN-C/rGO has 95% retention for disk current after 12 h testing indicating the high catalytic stability. The electrochemical surface area (ECSA) of BN-C/rGO is lower than that of rGO (Fig. S13) implying that the better catalytic performance is from the higher intrinsic activity of h-BN/G heterostructure rather than the various ECSAs [41,47]. Compared to the BN-C carbon dots, the BN-C/rGO has much higher ECSAs indicating the rGO substrate is beneficial to exposing more active sites of BN-C dots. In the Electrochemical Impedance Spectroscopy (EIS) in Fig. S14, compared to the BN-C dots and rGO, the BN-C/rGO exhibits a small semicircle indicative of the lower charge transfer resistance, which can be attributed to a good interfacial charge transfer between catalyst (BN-C dots) and conductive substrate (rGO) by the π-π conjugation [48]. We further optimized the BN-C carbon dots loading on rGO and the corresponding catalysts were named as BN-C/rGO-x (x, representing the volume ratio of BN-S dots solution/GO solution, x = 0.1, 0.4, 0.6, 1.0, See methods) in Fig. S15. The BN-C/rGO-x samples show a volcano curve when comparing the catalytic activity (represented by I_R) and HO_2^- selectivity against the volume ratio, and the BN-C/rGO-0.6 is found to be the optimal catalyst (Fig. 4 f).

In order to further demonstrate the key role of h-BN/G heterostructure, the B, N-C/rGO (adding B, N resources), B-C/rGO (only adding B resource), N-C/rGO (only adding N resource) and C/rGO (no adding B, N resources) were prepared and the catalytic performance was measured (Fig. S16 and Table 1). The 2 e⁻ ORR performance of C/rGO, B-C/rGO, N-C/rGO, and B, N-C/rGO can be attributed to fewer oxygen species and B, N doping [17,49]. Compared to the above four control catalysts in Table 1, the BN-C/rGO has the highest HO_2^- selectivity of over 90%, I_R max= 0.54 mA and E_{onset}= 0.78 V vs. RHE. We also
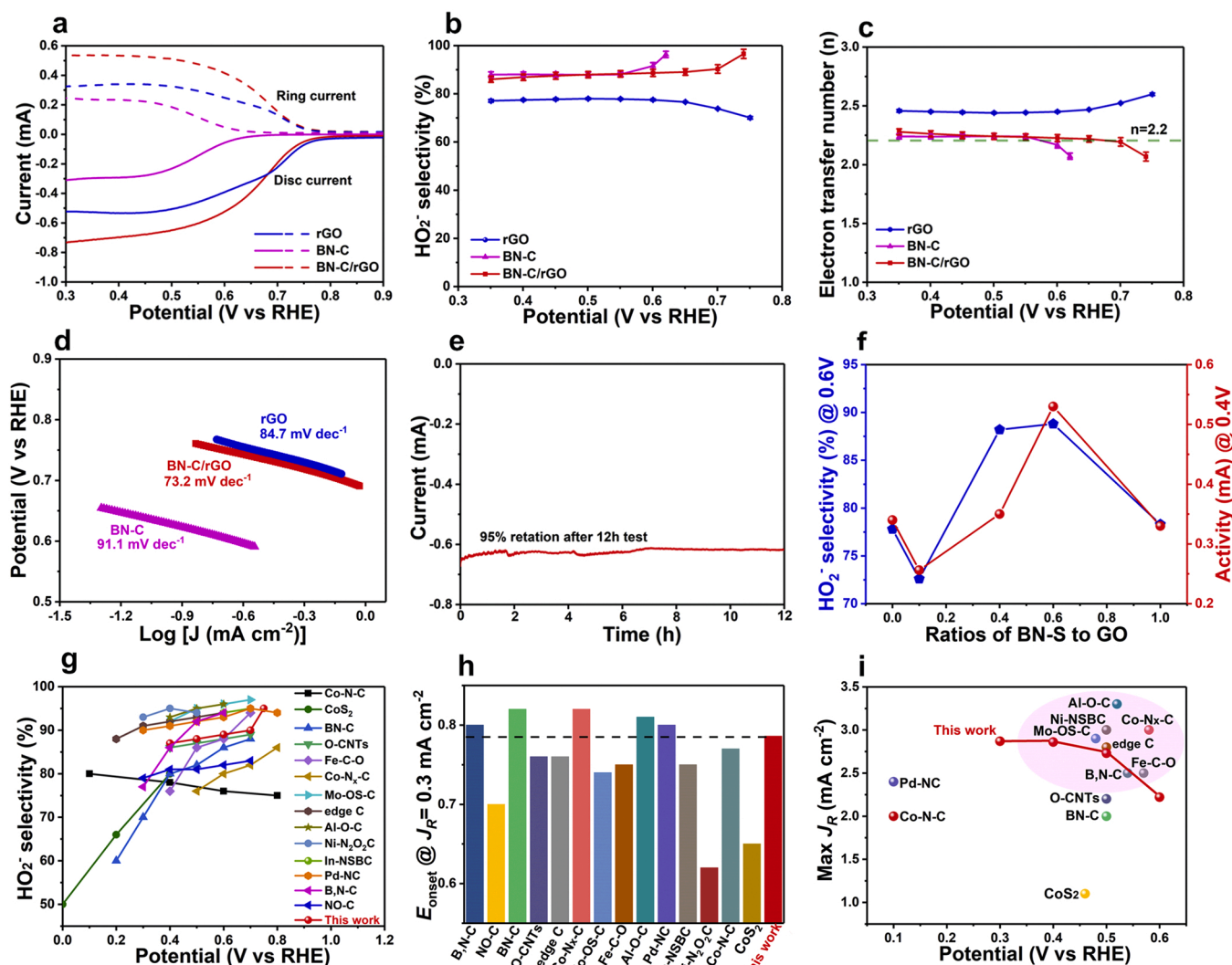
Fig. 4. (a) The LSV curves of rGO, BN-C carbon dots and BN-C/rGO (solid lines) together with the corresponding HO_2^- current on the ring electrode (dashed lines) at a fixed potential of 1.2 V vs. RHE in O_2-saturated 0.1 M KOH solution at 1600 rpm. (b, c) The calculated HO_2^- selectivity and electron transfer number (n) during the potential sweep. Three independent measurements of HO_2^- selectivity and the mean value of electron transfer number with error bar. (d) The Tafel curves derived from the LSV curves in (a). (e) The stability test of the BN-C/rGO at a fixed disk potential of 0.4 V vs. RHE at 1600 rpm. (f) The comparison of HO_2^- selectivity at 0.6 V vs. RHE and catalytic activity (represented by I_R) at 0.4 V vs. RHE for the BN-C/rGO with different pBN content. (g-i) The comparison of HO_2^- selectivity, onset potential, and maximal current density to the reported electrocatalysts in the alkaline environment.

Table 1
The summary of 2 e^- ORR performance for different control samples.

Samples	HO_2^- Sele.	max I_R (mA)[a]	E_{onset} (V vs. RHE)[b]
BN-C/rGO-0.6	**over 90%**	**0.54**	
			0.78
BN-C carbon dots	~90%	0.25	
			0.60
rGO	78%	0.33	
			0.78
C/rGO	56%	0.30	
			0.65
B-C/rGO	77%	0.33	
			0.68
N-C/rGO	83%	0.39	
			0.71
B, N-C/rGO	82%	0.34	
			0.68
pBN-C/rGO	85%	0.17	
			0.59

[a] The maximal ring current (max I_R) is determined according to the LSV curves.
[b] The E_{onset} is determined at the $J_R = 0.3$ mA cm^{-2}.

prepared the pBN-C/rGO without the ball milling process (the other conditions are the same as those of the BN-C/rGO). The pBN-C/rGO shows the HO_2^- selectivity= 85%, I_R max= 0.17 mA and E_{onset}= 0.59 V (Fig. S16). The much higher I_R max and E_{onset} in the BN-C/rGO than the pBN-C/rGO also demonstrates the greatly enhanced formation of h-BN/G heterostructure active sites upon ball milling treatment.

The reported electrocatalysts are summarized to compare their catalytic performance including HO_2^- selectivity, onset potential, and catalytic activity (represented by J_R) in Fig. 4g-i (see details in Table S1). In the range of 0.45–0.75 V vs. RHE (Fig. 4 g), the BN-C/rGO always shows high HO_2^- selectivity (88%−95%), superior to most of the reported electrocatalysts. Although many electrocatalysts have higher HO_2^- selectivity, their onset potentials are lower than our BN-C/rGO (0.78 V vs. RHE, determined $J_R = 0.3$ mA cm^{-2}) in Fig. 4 h. The maximal ring current density (max J_R) was summarized in Fig. 4i, and the max J_R of BN-C/rGO is up to 2.87 mA cm^{-2} which is lower than those of many metal-based electrocatalysts, but superior to the reported carbon-based electrocatalysts. Based on the above comprehensive comparisons, the BN-C/rGO with high 2 e^- ORR activity and selectivity is a promising metal-free carbon-based electrocatalyst for HO_2^- synthesis.
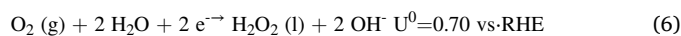
The BN-C/rGO catalyst was evaluated under high current density conditions for potential commercial application in a flow cell setup. As shown in Fig. 5a and Fig. S17, we assembled the flow cell integrating the BN-C/rGO coated (1 mg cm^{-2}) gas diffusion layer (GDL) as the cathode, Pt film as the anode, and Ag/AgCl as the reference electrode. The current density rapidly reaches to 100 mA cm^{-2} at -0.37 V vs. RHE in this flow cell (Fig. 5b). Compared to the bare GDL electrode, the loading of electrocatalyst results into the much higher current density, indicating the high catalytic performance of BN-C/rGO (Fig. S18). The catalytic stability was measured by the i-t curve at a fixed potential of 0.2 V vs. RHE corresponding to the current density of ~50 mA cm^{-2}, and we found the current density showed almost no change after 8 h testing (Fig. 5c). The HO$_2^-$ in the electrolyte was detected by the Ce^{4+} titration method (Fig. S19) and the HO$_2^-$ concentration gradually increased to 50 mM in 100 ml electrolyte (0.1 M KOH) by prolonging the reaction time to 8 h in Fig. 5d. The reaction rate is calculated to be up to 960 mmolg$_{catalyst}^{-1}$ h^{-1} in the initial 1 h testing which higher than most of the catalysts (Table S2). The Faradaic efficiency (FE%) of HO$_2^-$ (defined as the amount of charge producing HO$_2^-$/H$_2$O$_2$ versus the total charge used in H-cell or flow-cell measurements) is calculated to be over 90% at the initial 4 h and the FE% retains over 70% after 8 h testing. The retained FE% is higher than the reported electrocatalysts measured by a flow cell setup[45]. To explore the practical application of electrochemically synthesized HO$_2^-$, we added the electrolyte (12 ml, 50 mM HO$_2^-$) into a methylene blue (MB) solution (8 ml, 200 ppm). Then, the pH of the final solution was modulated to be 2.0. Fe^{2+} was added to induce the Fenton reaction leading to the formation of hydroxyl radical for degrading MB. In Fig. 5e, the typical absorption peaks of MB rapidly disappear in UV–vis spectra, and the mixture solution becomes colorless (inset in Fig. 5e). After the degrading progress, the residual MB cannot be detected in Fig. 5 f.

3.4. Catalytic sites determined by DFT simulation

To explore the origin of the active sites in the h-BN/G heterostructure dots, many simplified graphene quantum dot (GQDs) models were designed, and different h-BN domain sizes were doped into GQDs. The B or N doped GQD were added and compared (Fig. 6a) based on the previous models of B dopant and graphitic N dopant in graphene [17, 50]. All the potential active sites were determined based on the optimized adsorption configurations between the active site and of OOH* (key oxygenated intermediate, in 2 e$^-$ ORR), including B, N, C (nearby interfacial B or N) atoms (Fig. S20).

In the 2 e$^-$ ORR, O$_2$ is converted to H$_2$O$_2$ (Eq. 1). where U^0 is the equilibrium potential for this 2 e$^-$ pathway.

$$O_2 \text{ (g)} + 2 \text{ H}_2\text{O} + 2 \text{ e}^- \rightarrow \text{H}_2\text{O}_2 \text{ (l)} + 2 \text{ OH}^- \quad U^0 = 0.70 \text{ vs·RHE} \qquad (6)$$

It is generally accepted that the electroreduction of O$_2$ to H$_2$O$_2$ involves two coupled electrons:

$$O_2 + * + \text{H}_2\text{O} + \text{e}^- \rightarrow \text{OOH}* + \text{OH}^- \qquad (2)$$

$$\text{OOH}* + \text{H}_2\text{O} + \text{e}^- \rightarrow * + \text{H}_2\text{O}_2 \text{ (l)} + \text{OH}^- \qquad (3)$$

The reaction rate is greatly dependent on the reaction energy barrier of O$_2$ to OOH* (ΔG), and in the ideal model, the reaction free energies for all electron-transfer steps should be zero when the applied potential is equal to the equilibrium potential. In Fig. 6b, the ΔG of B doping (1B) and N doping (1 N) are 0.54 eV and 0.47 eV, respectively. For different size h-BN doping models, the ΔG of 1BN (one B-N pair), 3BN (three B-N pairs), 5BN (five B-N pairs), 9BN-B (nine B-N pairs) and 9BN-N are -0.25 eV, -0.17 eV, -0.09 eV, -1.10 eV, and 0.44 eV, respectively (Table S3). For the pure h-BN quantum dot model, the ΔG of Layering-BN-B and Layering-BN-N are -1.14 eV and 1.00 eV, respectively. Compared to the ΔG of all models, the 5BN model catalyst can achieve a higher reaction rate in the same condition due to its ΔG close to zero.
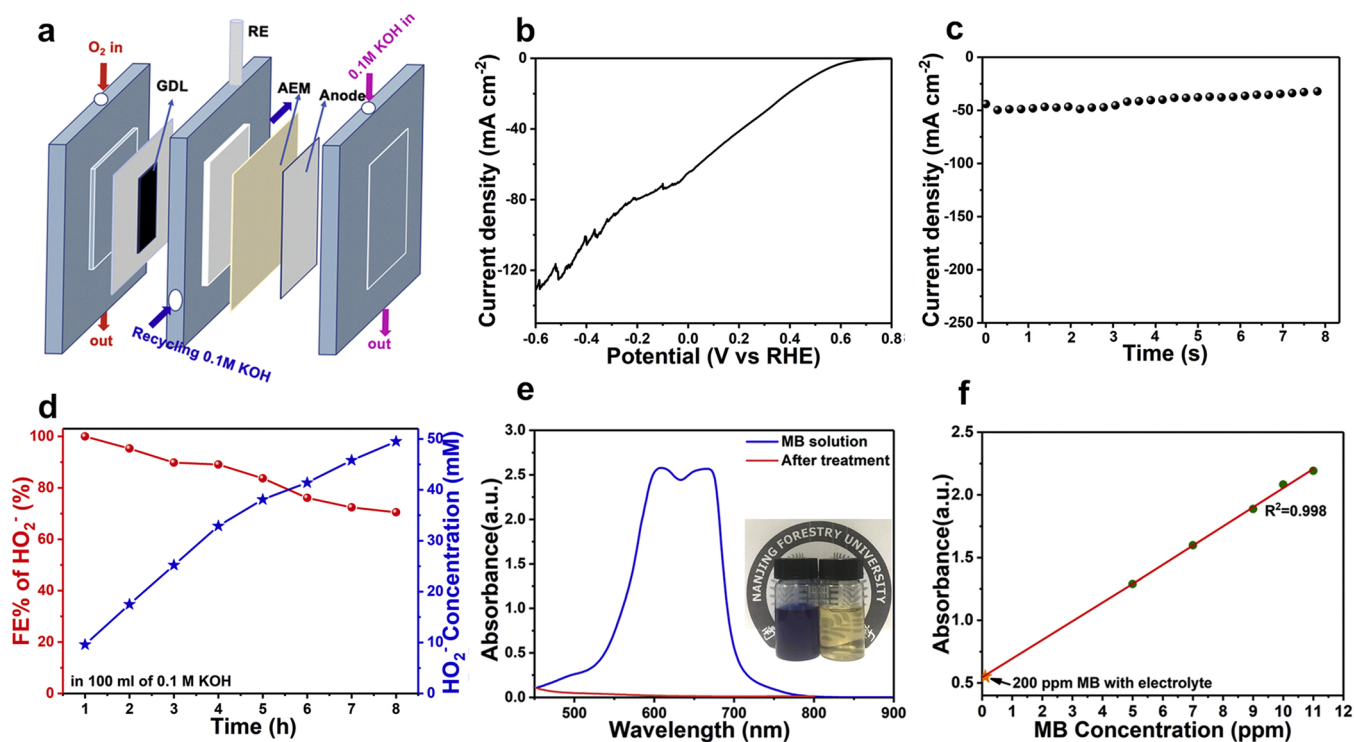

Fig. 5. (a) The schematic illustration of flow cell setup. (b) The LSV curve of flow cell setup with the BN-C/rGO as the catalyst in the cathode at the scan rate of 10 mV s^{-1}. (c) The i-t curve at 0.2 V vs. RHE for the HO$_2^-$ production in the flow cell. (d) The FE% of HO$_2^-$ and HO$_2^-$ concentration in the flow cell during 8 h testing. (e) The UV–vis spectra of MB solution before and after adding electrolyte (inset, the photograph of 200 ppm MB solution before and after treatment). (f) The fitting standard curve between MB concentration and absorbance (the orange pentagram represents the MB solution treated by the electrolyte).
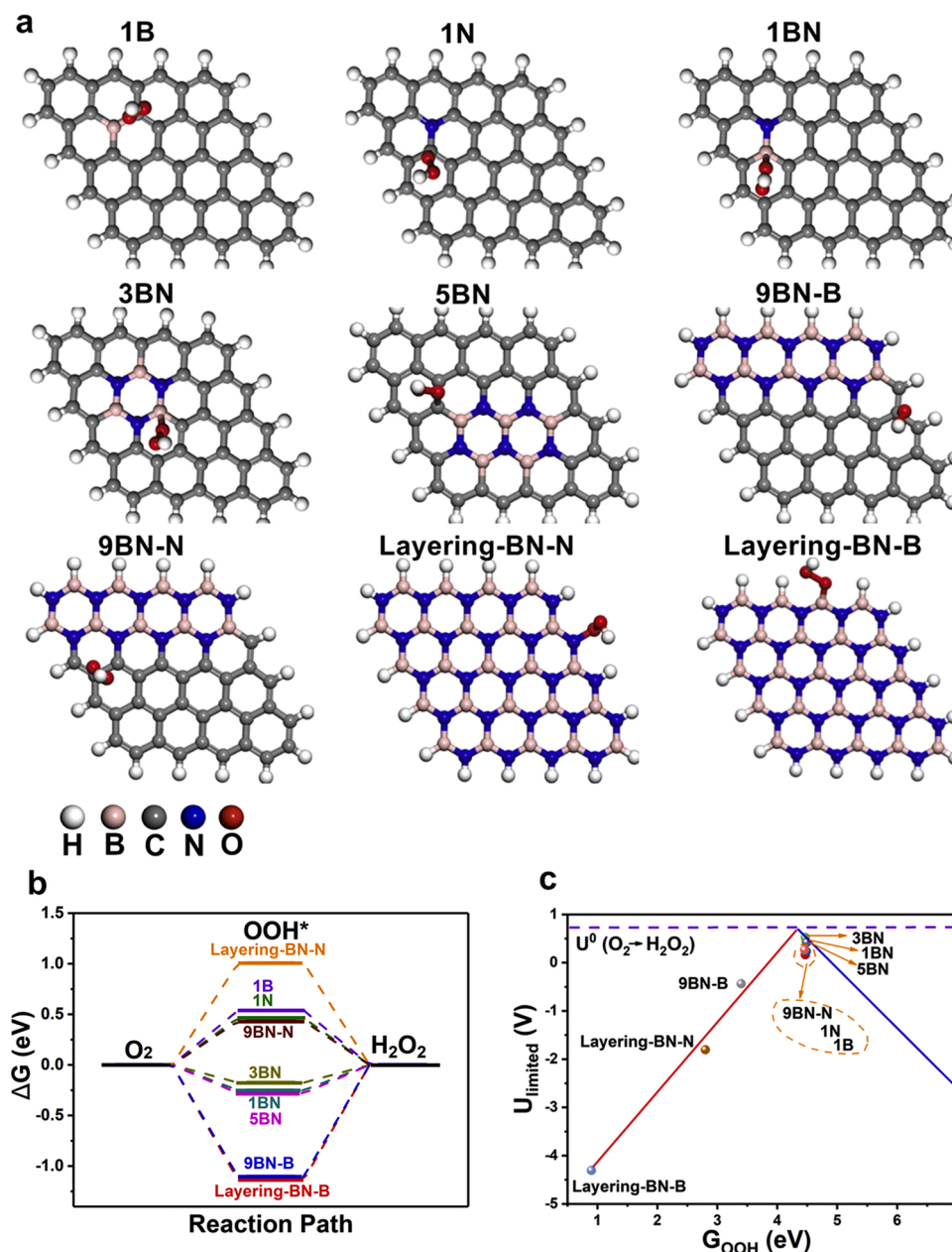
Fig. 6. (a) the optimized models with OOH* intermediates adsorption. (b) The illustration of 2 e⁻ ORR reaction pathway on the optimized models. (c) The volcano plot between ΔG_{OOH*} and the 2 e⁻ ORR $U_{limited}$ for the optimized models and the purple dotted line representing the equilibrium potential of O_2/H_2O_2.

The reaction rate order is 5BN > 3BN > 1BN > 1 N > 1B > 9BN-N.

The Gibbs free adsorption energy (ΔG_{OOH*}) for OOH* intermediate species on catalyst surface has been successfully employed as a descriptor for correlating with 2 e⁻ ORR theoretical predictions[51,52]. When the ΔG_{OOH*} of models are closest to the most suitable value (4.22 eV), it will reach the best $U_{limited}$ (0.70 eV) for producing H_2O_2. The $U_{limited}$ of pure h-BN GQD (Layering-BN-N and Layering BN-B) is far away from the volcanic map top and in the opposite, the planar h-BN/G heterostructure (1BN, 3BN, 5BN, 9BN), located near the volcano map top, have a robust performance where ΔG_{OOH*} for OOH* is around 4.4 eV (Fig. 6c). Therefore, those planar h-BN/G heterostructures are hopeful of becoming catalytic active sites which could provide a voltage close to the ideal 0.7 V vs. RHE[53]. Remarkably, compared to the reported B or N doped graphene, the $U_{limited}$ of planar h-BN/G heterostructure is closer to the top of volcano map, indicating higher catalytic activity.

The charge difference (Fig. S21) shows obvious electron transfer of

N, B (C) to form bonds. Through the systematic comparison of the above possible structure, the h-BN domain modified surface can effectively improve the electronic structure at the h-BN/G heterostructure. The deficient electrons around B atoms at the heterostructure are an important reason for h-BN/G to act as the active sites for the 2 e⁻ pathway.

4. Conclusion

In summary, we develop a new route for fabricating carbon dots containing h-BN/G heterostructure active sites for 2 e⁻ ORR by sucrose-assisted h-BN exfoliating followed by graphite growing process with h-BN nanodots as "seed nucleation". The BN-C carbon dots exhibits excellent catalytic performance of 2 e⁻ ORR and has high HO_2^- selectivity at low overpotentials. The BN-C carbon dots have a high production rate and FE% of HO_2^- in the flow cell, superior to the reported carbon-based electrocatalysts. Experimental results and DFT simulation demonstrated

that the high catalytic performance is derived from the electron-deficient B atoms at the h-BN/G interface. This work emphasizes the promise of heterostructure in carbon materials as efficient, selective, and productive active sites.

CRediT authorship contribution statement

Mengmeng Fan: Conceptualization, Methodology, Investigation, Writing – original draft. **Yuying Zhao:** Formal analysis. **Jingjie Wu:** Writing – review & editing. **Jithu Raj:** Writing – review & editing. **Zeming Wang:** Formal analysis. **Kang Sun:** Validation, Formal analysis, Investigation, Supervision. **Jianchun Jiang:** Writing – review & editing, Supervision.

Declaration of Competing Interest

The authors declare that they have no known competing financial interests or personal relationships that could have appeared to influence the work reported in this paper.

Data Availability

Data will be made available on request.

Supporting Information

Additional data including FT-IR spectrum, AFM image of BN-S dots, photograph of BN-C and BN-C/rGO, Nitrogen adsorption–desorption isotherms and the corresponding pore diameter distribution of BN-C and BN-C/rGO, HR-TEM images of C/rGO and B, N-C/rGO, XPS data, collecting efficiency of HO_2^-, catalytic properties of different samples and DFT simulation data.

Appendix A. Supporting information

Supplementary data associated with this article can be found in the online version at doi:10.1016/j.apcatb.2022.122195.

References

[1] C. Xia, Y. Xia, P. Zhu, L. Fan, H. Wang, Direct electrosynthesis of pure aqueous H_2O_2 solutions up to 20% by weight using a solid electrolyte, Science 366 (2019) 226–231.

[2] H.W. Kim, M.B. Ross, N. Kornienko, L. Zhang, J. Guo, P. Yang, B.D. McCloskey, Efficient hydrogen peroxide generation using reduced graphene oxide-based oxygen reduction electrocatalysts, Nat. Catal. 1 (2018) 282–290.

[3] J. Sun, Y. Wu, Anthraquinone redox relay for dye-sensitized photo-electrochemical H_2O_2 production, Angew. Chem. Int. Ed. 59 (2020) 10904–10908.

[4] Y. Xue, Y. Wang, Z. Pan, K. Sayama, Electrochemical and photoelectrochemical water oxidation for hydrogen peroxide production, Angew. Chem. Int. Ed. 60 (2021) 10469–10480.

[5] Y. Bu, Y. Wang, G.F. Han, Y. Zhao, X. Ge, F. Li, Z. Zhang, Q. Zhong, J.B. Baek, Carbon-based electrocatalysts for efficient hydrogen peroxide production, Adv. Mater. (2021), e2103266.

[6] N. Wang, S. Ma, P. Zuo, J. Duan, B. Hou, Recent progress of electrochemical production of hydrogen peroxide by two-electron oxygen reduction reaction, Adv. Sci. 8 (2021), e2100076.

[7] Q. Chang, P. Zhang, A.H.B. Mostaghimi, X. Zhao, S.R. Denny, J.H. Lee, H. Gao, Y. Zhang, H.L. Xin, S. Siahrostami, J.G. Chen, Z. Chen, Promoting H2O2 production via 2-electron oxygen reduction by coordinating partially oxidized Pd with defect carbon, Nat. Commun. 11 (2020) 2178.

[8] S. Yang, J. Kim, Y.J. Tak, A. Soon, H. Lee, Single-atom catalyst of platinum supported on titanium nitride for selective electrochemical reactions, Angew. Chem. Int. Ed. 55 (2016) 2058–2062.

[9] J.S. Jirkovský, I. Panas, E. Ahlberg, M. Halasa, S. Romani, D.J. Schiffrin, Single Atom hot-spots at Au–Pd nanoalloys for electrocatalytic H_2O_2 production, J. Am. Chem. Soc. 133 (2011) 19432–19441.

[10] T. Ricciardulli, S. Gorthy, J.S. Adams, C. Thompson, A.M. Karim, M. Neurock, D. W. Flaherty, Effect of Pd coordination and isolation on the catalytic reduction of O_2 to H_2O_2 over PdAu bimetallic nanoparticles, J. Am. Chem. Soc. 143 (2021) 5445–5464.

[11] Y. Xiao, J. Hong, X. Wang, T. Chen, T. Hyeon, W. Xu, Revealing kinetics of two-electron oxygen reduction reaction at single-molecule level, J. Am. Chem. Soc. 142 (2020) 13201–13209.

[12] F. Wu, C. Pan, C.-T. He, Y. Han, W. Ma, H. Wei, W. Ji, W. Chen, J. Mao, P. Yu, D. Wang, L. Mao, Y. Li, Single-atom Co–N_4 electrocatalyst enabling four-electron oxygen reduction with enhanced hydrogen peroxide tolerance for selective sensing, J. Am. Chem. Soc. 142 (2020) 16861–16867.

[13] M. Wang, N. Zhang, Y. Feng, Z. Hu, Q. Shao, X. Huang, Partially pyrolyzed binary metal–organic framework nanosheets for efficient electrochemical hydrogen peroxide synthesis, Angew. Chem. Int. Ed. 59 (2020) 14373–14377.

[14] C. Tang, Y. Jiao, B. Shi, J.-N. Liu, Z. Xie, X. Chen, Q. Zhang, S.-Z. Qiao, Coordination tunes selectivity: two-electron oxygen reduction on high-loading molybdenum single-atom catalysts, Angew. Chem. Int. Ed. 59 (2020) 9171–9176.

[15] Q. Yang, W. Xu, S. Gong, G. Zheng, Z. Tian, Y. Wen, L. Peng, L. Zhang, Z. Lu, L. Chen, Atomically dispersed Lewis acid sites boost 2-electron oxygen reduction activity of carbon-based catalysts, Nat. Commun. 11 (2020) 5478.

[16] D. Iglesias, A. Giuliani, M. Melchionna, S. Marchesan, A. Criado, L. Nasi, M. Bevilacqua, C. Tavagnacco, F. Vizza, M. Prato, P. Fornasiero, N-doped graphitized carbon nanohorns as a forefront electrocatalyst in highly selective O_2 reduction to H_2O_2, Chem 4 (2018) 106–123.

[17] Y. Xia, X. Zhao, C. Xia, Z.-Y. Wu, P. Zhu, J.Y. Kim, X. Bai, G. Gao, Y. Hu, J. Zhong, Y. Liu, H. Wang, Highly active and selective oxygen reduction to H_2O_2 on boron-doped carbon for high production rates, Nat. Commun. 12 (2021) 4225.

[18] Z. Lu, G. Chen, S. Siahrostami, Z. Chen, K. Liu, J. Xie, L. Liao, T. Wu, D. Lin, Y. Liu, T.F. Jaramillo, J.K. Nørskov, Y. Cui, High-efficiency oxygen reduction to hydrogen peroxide catalysed by oxidized carbon materials, Nat. Catal. 1 (2018) 156–162.

[19] L. Han, Y. Sun, S. Li, C. Cheng, C.E. Halbig, P. Feicht, J.L. Hübner, P. Strasser, S. Eigler, In-plane carbon lattice-defect regulating electrochemical oxygen reduction to hydrogen peroxide production over nitrogen-doped graphene, ACS Catal. 9 (2019) 1283–1288.

[20] Y.J. Sa, J.H. Kim, S.H. Joo, Active edge-site-rich carbon nanocatalysts with enhanced electron transfer for efficient electrochemical hydrogen peroxide production, Angew. Chem. Int. Ed. 58 (2019) 1100–1105.

[21] M.A. Ahsan, T. He, K. Eid, A.M. Abdullah, M.L. Curry, A. Du, A.R. Puente Santiago, L. Echegoyen, J.C. Noveron, Tuning the intermolecular electron transfer of low-dimensional and metal-free BCN/C_{60} electrocatalysts via interfacial defects for efficient hydrogen and oxygen electrochemistry, J. Am. Chem. Soc. 143 (2021) 1203–1215.

[22] M. Fan, J. Wu, J. Yuan, L. Deng, N. Zhong, L. He, J. Cui, Z. Wang, S.K. Behera, C. Zhang, J. Lai, B.I. Jawdat, R. Vajtai, P. Deb, Y. Huang, J. Qian, J. Yang, J. M. Tour, J. Lou, C.-W. Chu, D. Sun, P.M. Ajayan, Doping nanoscale graphene domains improves magnetism in hexagonal boron nitride, Adv. Mater. 31 (2019) 1805778.

[23] R. Kumar, S. Sahoo, E. Joanni, R.K. Singh, R.M. Yadav, R.K. Verma, D.P. Singh, W. K. Tan, A. Pérez del Pino, S.A. Moshkalev, A. Matsuda, A review on synthesis of graphene, h-BN and MoS_2 for energy storage applications: Recent progress and perspectives, Nano Res 12 (2019) 2655–2694.

[24] M. Fan, Z. Wang, Y. Zhao, Q. Yuan, J. Cui, J. Raj, K. Sun, A. Wang, J. Wu, H. Sun, B. Li, L. Wang, J. Jiang, Porous heterostructure of graphene/hexagonal boron nitride as an efficient electrocatalyst for hydrogen peroxide generation, Carbon Energy (2022), https://doi.org/10.1002/cey2.309.

[25] T. Zhang, W. Li, K. Huang, H. Guo, Z. Li, Y. Fang, R.M. Yadav, V. Shanov, P. M. Ajayan, L. Wang, C. Lian, J. Wu, Regulation of functional groups on graphene quantum dots directs selective CO_2 to CH_4 conversion, Nat. Commun. 12 (2021) 5265.

[26] L. Wang, Y. Wang, T. Xu, H. Liao, C. Yao, Y. Liu, Z. Li, Z. Chen, D. Pan, L. Sun, M. Wu, Gram-scale synthesis of single-crystalline graphene quantum dots with superior optical properties, Nat. Commun. 5 (2014) 5357.

[27] Q. Li, M. Liu, Y. Zhang, Z. Liu, Hexagonal boron nitride–graphene heterostructures: synthesis and interfacial properties, Small 12 (2016) 32–50.

[28] D. Li, B. Wang, X. Long, W. Xu, Y. Xia, D. Yang, X. Yao, Controlled asymmetric charge distribution of active centers in conjugated polymers for oxygen reduction, Angew. Chem. Int. Ed. 60 (2021) 26483–26488.

[29] L. Chen, X. Wang, Bio-templated fabrication of metal-free boron carbonitride tubes for visible light photocatalysis, Chem. Commun. 53 (2017) 11988–11991.

[30] W. Lei, D. Portehault, R. Dimova, M. Antonietti, Boron carbon nitride nanostructures from salt melts: tunable water-soluble phosphors, J. Am. Chem. Soc. 133 (2011) 7121–7127.

[31] S. Chen, R. Xu, J. Liu, X. Zou, L. Qiu, F. Kang, B. Liu, H.M. Cheng, Simultaneous production and functionalization of boron nitride nanosheets by sugar-assisted mechanochemical exfoliation, Adv. Mater. 31 (2019), e1804810.

[32] Y. Xu, K. Sheng, C. Li, G. Shi, Self-assembled graphene hydrogel via a one-step hydrothermal process, ACS Nano 4 (2010) 4324–4330.

[33] M.A. Augustyniak-Jabłokow, R. Strzelczyk, R. Fedaruk, Localization of conduction electrons in hydrothermally reduced graphene oxide: electron paramagnetic resonance studies, Carbon 168 (2020) 665–672.

[34] M. Fan, C. Zhu, J. Yang, D. Sun, Facile self-assembly N-doped graphene quantum dots/graphene for oxygen reduction reaction, Electrochim. Acta 216 (2016) 102–109.

[35] H. Li, R.Y. Tay, S.H. Tsang, X. Zhen, E.H. Teo, Controllable Synthesis of Highly Luminescent Boron Nitride Quantum Dots, Small 11 (2015) 6491–6499.

[36] P. Thangasamy, M. Santhanam, M. Sathish, Supercritical fluid facilitated disintegration of hexagonal boron nitride nanosheets to quantum dots and its application in cells imaging, ACS Appl. Mater. Inter. 8 (2016) 18647–18651.

[37] X. Song, T. Gao, Y. Nie, J. Zhuang, J. Sun, D. Ma, J. Shi, Y. Lin, F. Ding, Y. Zhang, Z. Liu, Seed-assisted growth of single-crystalline patterned graphene domains on hexagonal boron nitride by chemical vapor deposition, Nano Lett. 16 (2016) 6109–6116.

[38] Y. Han, B. Tang, L. Wang, H. Bao, Y. Lu, C. Guan, L. Zhang, M. Le, Z. Liu, M. Wu, Machine-learning-driven synthesis of carbon dots with enhanced quantum yields, ACS Nano 14 (2020) 14761–14768.

[39] L. Cao, P. Dai, J. Tang, D. Li, R. Chen, D. Liu, X. Gu, L. Li, Y. Bando, Y.S. Ok, X. Zhao, Y. Yamauchi, Spherical superstructure of boron nitride nanosheets derived from boron-containing metal–organic frameworks, J. Am. Chem. Soc. 142 (2020) 8755–8762.

[40] M. Zheng, T. Yuan, J. Shi, W. Cai, X. Wang, Photocatalytic oxygenation and deoxygenation transformations over BCN nanosheets, ACS Catal. 9 (2019) 8068–8072.

[41] M. Fan, Q. Yuan, Y. Zhao, Z. Wang, A. Wang, Y. Liu, K. Sun, L. Wang, J. Wu, J. Jiang, A facile "double catalysts" approach to directionally fabricate pyridinic N-B pair doped crystal graphene nanoribbons/amorphous carbon hybrid electrocatalysts for efficient oxygen reduction reaction, Adv. Mater. (2022), e2107040.

[42] G. Kim, S.-S. Kim, J. Jeon, S.I. Yoon, S. Hong, Y.J. Cho, A. Misra, S. Ozdemir, J. Yin, D. Ghazaryan, M. Holwill, A. Mishchenko, D.V. Andreeva, Y.-J. Kim, H.Y. Jeong, A. R. Jang, H.-J. Chung, A.K. Geim, K.S. Novoselov, B.-H. Sohn, H.S. Shin, Planar and van der Waals heterostructures for vertical tunnelling single electron transistors, Nat. Commun. 10 (2019) 230.

[43] M. Liu, Y. Xu, Y. Wang, X. Chen, X. Ji, F. Niu, Z. Song, J. Liu, Boron nitride quantum dots with solvent-regulated blue/green photoluminescence and electrochemiluminescent behavior for versatile applications, Adv. Opt. Mater. 5 (2017) 1600661.

[44] E. Jung, H. Shin, B.-H. Lee, V. Efremov, S. Lee, H.S. Lee, J. Kim, W. Hooch Antink, S. Park, K.-S. Lee, S.-P. Cho, J.S. Yoo, Y.-E. Sung, T. Hyeon, Atomic-level tuning of Co–N–C catalyst for high-performance electrochemical H$_2$O$_2$ production, Nat. Mater. 19 (2020) 436–442.

[45] S. Chen, T. Luo, K. Chen, Y. Lin, J. Fu, K. Liu, C. Cai, Q. Wang, H. Li, X. Li, J. Hu, H. Li, M. Zhu, M. Liu, Chemical identification of catalytically active sites on oxygen-doped carbon nanosheet to decipher the high activity for electro-synthesis hydrogen peroxide, Angew. Chem. Int. Ed. 60 (2021) 16607–16614.

[46] H. Fei, R. Ye, G. Ye, Y. Gong, Z. Peng, X. Fan, E.L.G. Samuel, P.M. Ajayan, J. M. Tour, Boron- and nitrogen-doped graphene quantum dots/graphene hybrid nanoplatelets as efficient electrocatalysts for oxygen reduction, ACS Nano 8 (2014) 10837–10843.

[47] L. Jiao, J. Zhu, Y. Zhang, W. Yang, S. Zhou, A. Li, C. Xie, X. Zheng, W. Zhou, S.-H. Yu, H.-L. Jiang, Non-bonding interaction of neighboring Fe and Ni single-atom pairs on MOF-derived N-doped carbon for enhanced CO$_2$ electroreduction, J. Am. Chem. Soc. 143 (2021) 19417–19424.

[48] T. Van Tam, S.G. Kang, K.F. Babu, E.-S. Oh, S.G. Lee, W.M. Choi, Synthesis of B-doped graphene quantum dots as a metal-free electrocatalyst for the oxygen reduction reaction, J. Mater. Chem. A 5 (2017) 10537–10543.

[49] J. Han, G. Huang, Z. Wang, Z. Lu, J. Du, H. Kashani, M. Chen, Low-temperature carbide-mediated growth of bicontinuous nitrogen-doped mesoporous graphene as an efficient oxygen reduction electrocatalyst, Adv. Mater. 30 (2018) 1803588.

[50] J. Zhang, G. Zhang, S. Jin, Y. Zhou, Q. Ji, H. Lan, H. Liu, J. Qu, Graphitic N in nitrogen-Doped carbon promotes hydrogen peroxide synthesis from electrocatalytic oxygen reduction, Carbon 163 (2020) 154–161.

[51] Z. Wang, Q.-K. Li, C. Zhang, Z. Cheng, W. Chen, E.A. McHugh, R.A. Carter, B. I. Yakobson, J.M. Tour, Hydrogen peroxide generation with 100% faradaic efficiency on metal-free carbon black, ACS Catal. 11 (2021) 2454–2459.

[52] X. Tan, H.A. Tahini, S.C. Smith, Understanding the high activity of mildly reduced graphene oxide electrocatalysts in oxygen reduction to hydrogen peroxide, Mater. Horiz. 6 (2019) 1409–1415.

[53] S. Siahrostami, A. Verdaguer-Casadevall, M. Karamad, D. Deiana, P. Malacrida, B. Wickman, M. Escudero-Escriban, E.A. Paoli, R. Frydendal, T.W. Hansen, I. Chorkendorff, I.E.L. Stephens, J. Rossmeisl, Enabling direct H$_2$O$_2$ production through rational electrocatalyst design, Nat. Mater. 12 (2013) 1137–1143.